Scientific Review
ISSN(e): 2412-2599, ISSN(p): 2413-8835
Vol. 5, Issue. 2, pp: 33-44, 2019
URL: https://arpgweb.com/journal/journal/10
DOI: https://doi.org/10.32861/sr.52.33.44

Academic Research Publishing Group

Original Research **Open Access**

Study of Microstructural, Electrical and Dielectric Properties of $La_{0.9}Pb_{0.1}MnO_3$ and $La_{0.8}Y_{0.1}Pb_{0.1}MnO_3$ Ceramics

S. A. Saleh
Physics Department, Faculty of Science, Sohag University, Sohag 82524, Egypt
Physics Department, College of Science & Arts, Najran University, P. O. 1988 Najran, KSA.

Abstract

The present work studies the microstructural and electrical properties of $La_{0.9}Pb_{0.1}MnO_3$ and $La_{0.8}Y_{0.1}Pb_{0.1}MnO_3$ ceramics synthesized by solid-state route method. Microstructure and elemental analysis of both samples were carried out by field emission scanning electron microscope (FESEM) and energy dispersive spectroscopy (EDS) method, respectively. Phase analysis by X-ray diffraction (XRD) indicated formation of single phase distorted structure. The XRD data were further analyzed by Rietveld refinement technique. Raman analysis reveals that Y atom substitutes La site into the LPMO with shifting of phonon modes. The temperature variation of resistivity of undoped and Y-doped $La_{0.9}Pb_{0.1}MnO_3$ samples have been investigated. The electrical resistivity as a function of temperature showed that all samples undergo an metal-insulator (M-I) transition having a peak at transition temperature T_{MI}. Y-doping increases the resistivity and the metal-insulator transition temperature (T_{MI}) shifts to lower temperature. The temperature-dependent resistivity for temperatures less than metal-insulator transition is explained in terms the quadratic temperature dependence and for T > TMI, thermally activated conduction (TAC) is appropriate. Variation of frequency dispersion in permittivity and loss pattern due to La-site substitution in LPMO was observed in the dielectric response curve.

Keywords: Ceramics; Microstructure; Raman Scattering; Electrical resistivity; Dielectric constants.

1. Introduction

Recently, much attention have been paid to electroceramics due to their peculiar properties and potential applications in capacitors and memory devices. For capacitive and memory devices, in spite of magneto-electric effects, ceramics should have colossal dielectric constant (CDC) [1, 2]. Lead doped lanthanum manganite (LPMO), a typical perovskite oxide, shows exotic properties such as ferroelectric, antiferromagnetism and their coupling effects [3-9], which may be used in multifunctional device applications [10].

From among, the large number of papers dealing with their investigation, however, only a few were devoted to the dielectric properties, although the study of dielectric properties produces valuable information on the behavior of localized electric charge carriers leading to greater understanding of the mechanism of dielectric polarization in a material. Furthermore, the study on dielectric properties of the materials is expected not only to reveal comprehensive knowledge about the nature and origin of the loss occurring in these compounds as well as conduction mechanism but also provide information on the structural aspects of compositions [11]. Thus, an investigation on the relationship between the composition and dielectric properties of this material was seen important.

As with the perovskites, LPMO exhibits rich and interesting physical properties because of the strong interplay between lattice distortions, transport properties, and magnetic ordering. Additionally, LPMO is chemically and mechanically very stable and exhibits ferroelectric properties at and above room temperature, and finally it can be easily prepared and used in the form of ceramics. LPMO possesses ferromagnetic metallic ground state at RT, which is a useful property for application in devices and sensors. From view point of the applications, a high dielectric constant and a low dielectric loss are generally required together with an AC conductivity. Hence, the study of dielectric properties produce valuable information on the behavior of localized electric charge carriers leading to greater understanding of the mechanism of dielectric polarization in the investigated samples.

In the present work, the crystal structures, microstructures, compositions, electrical resistivity as well as dielectric studies were performed. Here, LPMO and LYPMO ceramics were synthesized by solid state reaction route. Infrared spectroscopy and Raman scattering in addition to the XRD and FESEM were used to study the structure of pure and yttrium substituted ceramics. The electrical resistivity together with dielectric properties of the present ceramics are characterized.

1.1. Experimental and Computational Details

The polycrystalline samples with the formulation of $La_{0.9}Pb_{0.1}MnO_3$ (LPMO) and $La_{0.8}Y_{0.1}Pb_{0.1}MnO_y$ (LYPMO) were prepared by standard ceramic method. The highly purified powders (99.9%) of La_2O_3, Y_2O_3, $MnCO_3$ and $PbCO_3$ were used as starting materials. All the chemicals were used without any further purification. All the starting materials were weighed, mixed and grounded thoroughly in an agate mortar. The homogeneous mixed powders were calcined at 900 ^oC for 24h and then cooled to room temperature. The calcined powders were uniaxially dye-pressed

at 5- 7 tonnes to form 2 mm thick and 15 mm diameter pellets and heated again at 1000 ^{o}C for 10 h. The crystalline phase, structure and particle size of both samples were obtained by means of X-ray diffraction (XRD) using a PANalytical X'Pert PRO diffractometer at room temperature with Cu (K_{α}) radiation (λ=1.5406Å) in 2θ range from 20 ^{o} to 80 ^{o}. Later on, the Rietveld refinements have been performed using FullPROF program to determine the diffraction parameters [12]. For Rietveld refinements, the XRD data were collected over the range of 2θ = 10–100˚ with a step width of 0.021 and a count time of 1s. The particle size and morphology were obtained by a field emission scanning electron microscope (FE-SEM: JEOL JSM-7600F). The elemental constituent was determined by using energy dispersive spectroscopy (EDS) attached to FE-SEM. Raman studies were performed using Perkin Elmer, Raman spectrometer with an excitation wavelength at 514.5 nm using an Ar laser. The bonding between different atoms and chemical information of the particles was collected by FT-IR spectra (Perkin Elmer). The FTIR spectra from the powders were obtained by the usual method of pressing them into KBr pellets. A conventional four probe technique was used for resistivity measurements in the temperature range of room temperature to 573 K. The dielectric characteristics at room temperature were carried out in the frequency range 75kHz-7MHz using an inductance-capacitance-resistance (LCR) meter (HP4284A).

2. Results and Discussion

2.1. Microstructure and Crystal Structure

The microstructure and particle size of LPMO and LYPMO samples, revealed by FESEM, are shown in Fig. 1. Overall, FESEM images show that various sizes of grains are randomly distributed and uniform grain size with significant pores is formed for both samples that one can observe clear grain boundaries. The micrographs suggest that materials comprise of polycrystalline microstructure and the percentage of doping affect the microstructure. The obtained micrographs show thin and appreciably fine flake-like structure $La_{0.9-x}Y_xPb_{0.1}MnO_3$ doping with Y^{3+} slightly reduces the grain size i.e. substitution of Y for La leads to a reduction in grain size. The decrease in grain size of the LYPMO might be interpreted in terms of the suppression of the oxygen vacancy concentration, which slows oxygen ion motion and consequently reduces the grain growth [13]. The corresponding EDS spectra of both samples are presented in Fig. 2. The analysis of the chemical composition of fabricated samples showed consistency with the molar ratio of $La_{0.9}Pb_{0.1}MnO_3$ and $La_{0.8}Y_{0.1}Pb_{0.1}MnO_3$. Moreover, the synthesized samples contain all La, Y, Pb, Mn and O elements which confirm that there is no loss of any integrated element during sintering and show a nominal composition near the desired one.

The powder XRD patterns of both samples are recorded at room temperature and are displayed in Fig. 3. The diffraction peaks observed in each sample show that the investigated samples are polycrystalline in nature. It is obvious that specimens possess a single phase corresponding to the rhombohedral crystal structure with space group $R\bar{3}c$ (No. 167) without any additional secondary phase within the sensitivity limits of the experiment. All the peaks in the patterns are perfectly match with the standard JCPDS card (JCPDS card no.98-009-5501) and they were consistent with the literature data [14, 15]. The results indicated that Y could be incorporated into the lattice of $La_{0.9}Pb_{0.1}MnO_3$ without affecting the rhombohedral structure. Moreover, the peak positions shifted slightly to higher angle due to the partial substitution of smaller ion Y^{3+} on the La^{+3} site. The results proved that the incorporation of Y ions led to lattice deformation due to the difference between ionic radius of La (138 pm) and Y (116 pm) [16]. All of results indicated that Y ions entered the crystal lattice of $La_{0.9}Pb_{0.1}MnO_3$ without deteriorating the original crystal structure.

The lattice parameters (*a* and *c*) of the rhombohedral structure of pure and Y-doped LPMO were estimated using the Miller indices (*hkl*) and the interplaner spacing (*d*) according to the relation [17]:

$$\frac{1}{d^2_{(hkl)}} = \frac{4}{3}\left(\frac{h^2+hk+k^2}{a^2}\right)+\frac{l^2}{c^2},$$

$$\sin^2\theta = \frac{\lambda^2}{4}\left\{\frac{4}{3}\left(\frac{h^2+hk+k^2}{a^2}\right)+\frac{l^2}{c^2}\right\}$$

According to the above formulas, for the (1 1 0) orientation at 2θ = 32.4201˚, the lattice constant *a* was calculated by $a = \frac{\lambda}{\sin\theta}$, and for (1 0 4) orientation at 2θ = 32.725˚, the lattice constant *c* was calculated by

$$c = \sqrt{\frac{12a^2\lambda^2}{3a^2\sin^2\theta-\lambda^2}}.$$

In order to ensure an accurate determination of unit cell parameters, the structure refinement was performed in the hexagonal setting of the rhombohedral $R\bar{3}c$ (Z= 6) space group, in which La/Y/Pb atoms are 6a (0,0,0.25) position, Mn at 6b (0,0,0) and O at 18e (x,0,0.25) position. The actual data (crosses), the calculated curve and difference profiles of the Rietveld refinement X-ray diffraction data of the samples are plotted in Fig. 4. Well agreement between the calculated and the observed data is obtained which confirms that the samples are prepared

without any other secondary or impurity phase. The unit cell parameters were obtained using the Rietveld refinement technique and are presented in Table 1 along with the values of the goodness-of-fit factor (GOF), the residual factor R_p and the weighted residual factor R_{wp}.

The average crystalline size (D_{hkl}) can be obtained by the X-ray line width using Scherrer's formula, $D_{hkl} = \frac{0.89\lambda}{\beta \cos\theta}$, where λ is the wavelength of X-rays used, β is the actual FWHM due to D_{hkl} only, which has been evaluated by taking into account the instrumental as well as the microstrain broadening and θ is the angle of diffraction [18]. The estimated average crystalline sizes are ~ 23 nm and ~20 nm for the non- substituted and substituted samples, respectively. This implies that the final powder is more towards nanosized than the bulk and this well supported by scanning electron microscopy. The data show that the presence of Y^{3+} ions in $La_{0.9}Pb_{0.1}MnO_3$ prevented the growth of crystal grains. XRD patterns also exhibit that as the Y content increases, the intensity of XRD peaks decreases and FWHM increases which shows the degradation of crystallinity and decrease in crystallite size. It means that the Y^{3+} ions occupy the regular lattice site of La^{3+}, they produce crystal defects around the dopants and the charge imbalance also arises.

It is seen that the lattice parameters decrease from a = 5.5002-5.4944Å and c = 13.3351(4)-13.3264 Å with enhanced Y doping concentration. A similar feature is observed for the unit-cell volume as shown in Table 1, indicating that the lattice shrinks and the unit cell becomes smaller with increasing Y concentration. The compression of lattice is attributed to the fact that the doping of Y at La site essentially produces Mn^{4+} with smaller ionic radii of (0.53 Å) as compared to Mn^{3+} ion (ionic radii 0.645 Å). Furthermore, the ratio of Mn^{4+}/Mn^{3+} gets changed after doping leading to presence of extra holes as charge carriers and thus improved conductivity. The presence of smaller ionic radii cations in the B sublattice of the ABO_3 perovskite is responsible for the reduction in unit cell volume leading to lattice distortions.

Another possible origin of the lattice distortion is the average ionic radius of the A-site element, which is governed by the tolerance factor. As t is close to unity, the cubic perovskite structure is realized. Furthermore, if $\langle r_A \rangle$ decreases, t also does, the lattice structure transforms to the rhombohedral ($0.96 < t < 1$) and then to the orthorhombic structure ($t < 0.96$), in which the bending of Mn-O-Mn bond and the deviating of the bond angle from 180° increase. For LYPMO, the ionic size of Y^{3+} is smaller than that of La^{3+}, which results in the tolerance factor t and it is larger than 0.96. On increasing Y content, both the Mn-O-Mn bond angle and the tolerance factor show an increasing trend, resulting in the crystal structure transforms to cubic-like symmetry. Based on structural results of Y-doping systems, it is inferred that the structure symmetry of doped perovskite manganites is affected by the size of doped ions. On the other hand, with doping of Y the angle between localized spins decrease (as the ionic radius of Y is smaller than that of La) very slightly. As a matter of fact, the effect of the decrease of tolerance factor dominates over the effect of the decrease of angle between the localized spins [19].

Raman scattering is known to be a powerful technique for the investigation of even subtle structural distortions and ferroelectric polarization both within a space group (via band shifts) or due to a phase transition (via band splitting and/or soft modes etc.). Hence, to obtain information about sample quality as well as position of the doping ions in the host lattice and probe the presence of impurities which are undetectable by X-ray analysis [20], Raman spectroscopy has been used. Pure and Y doped LPMO crystallize in rhombohedral crystal structure, with space group D_{3d}^6 ($R\bar{3}c$). For $R\bar{3}c$ rhombohedral structure, 30 normal modes at the zone center are known and five modes are Raman active modes. The classifications of Raman-active modes are $1A_{1g}+1E_g$ as rotational or tilt modes; $1E_g$ bending and $1E_g$ antistretching of MnO_6 octahedra and the remaining E_g is related to a vibration of A ions [21]. Moreover, it is well known that parent LPMO yields 13 Raman active phonon modes with distorted rhombohedral structure can be summarized using the irreducible representation $\Gamma_{Raman} = 4A_1 + 9E$ [22]. However, not all modes can be clearly observed at room temperature [23]. It is found that the A_{1g} mode involves the motion of the oxygen ions only in the C_2 sites, while the E_g modes arise both from the oxygen site and La site vibrations. The room temperature Raman spectra of LPMO and LYPMO ceramics in the frequency range 100-800 cm^{-1} are presented in Fig. 5. These Raman spectra reveals three broad bands and spectral maxima are mainly located in the interval of 170–220 cm^{-1}, 420–490 cm^{-1} and 550–650 cm^{-1} [24]. Generally, careful analyses of the spectra indicate appearance of more than one mode for each observed band. The lowest frequency band induced at 170–220 cm^{-1} has been assigned to the to the A_{1g} mode, while the highest frequency band at 550-650 cm^{-1} corresponds to symmetric stretching of the basal oxygen ion. The (420-490 cm^{-1}) band has been attributed to oxygen bending mode. The vibration modes observed near 185, 304, 467, 500, and 620 cm^{-1} are in agreement with the reported values in other works and definitely come from rhombohedral manganites [24-29]. In order to obtain each Raman active mode, the measured spectra were fitted, and the fitted curves were decomposed into individual Lorentzian components. Representative fitted spectra for $La_{1-x}Y_xPb_{0.1}MnO_3$ (x = 0.0, and 0.1) revealed five phonon modes as shown in Fig. 6. Usually rhombohedral structure illustrates five Raman active modes. It is noticed that the initial two modes show a shift of the peak position to higher frequencies, while to that latter three modes to lower frequencies with increasing Y concentration; reflecting the replacement of La ions with smaller Y ions causes significant changes in the environments surrounding the MnO_6 octahedra [30]. Also, it is evident that the width and intensity get stronger and stronger with increasing yttrium content.

Fourier transform infrared spectroscopy (FTIR) is one of the preferred methods of infrared spectroscopy. It was usually employed as an additional probe to identify the functional groups on the surface of synthesized samples. FTIR spectra were recorded in solid phase using KBr pellet technique in the wave number range of 4000‑400 cm^{-1} are shown in Fig. 7. The IR bands of solids located in the spectral range (1000-400 cm^{-1}) are usually assigned to

vibrations of ions in the crystal lattice [31]. The characteristic IR peaks in the range of 400-720 cm^{-1} is very important to study the presence or absence of Mn-O/La(Pb/Y)-O bonds and the functional groups. The very strong absorption bands observed around 600 cm^{-1} are attributed to the stretching modes of La-Pb-Mn-O. The absorptions centered at 450 cm^{-1} for pure LPMO can be assigned to the bending vibration. The main absorption band around 595 cm^{-1} corresponds to stretching of the metal-oxygen bond in the perovskite, which involves the internal motion of a change in Mn-O-Mn bond length in MnO_6 octahedral [32]. The strong band appearing around 600 cm^{-1} can be attributed to the Mn-O stretching vibration mode, ν_s, which involves the internal motion of a change in Mn-O bond length [33]. No additional absorption peaks were observed with Y addition, indicating homogeneous dispersion of dopant in the support material. Shifting of this band as a result of Y doping suggests microstructural changes taking place in the LPMO matrix. The stretching mode is related to the change of Mn-O-Mn bond length and the bending mode involves the change of Mn-O-Mn bond angle. The appearance of the stretching and bending modes at transmission spectra indicates that the perovskite structure of LSMO has been formed, which is in agreement with the result of XRD. In the 1000–4000 cm^{-1} range, the observed absorption bands can be attributed to the presence of some organic impurity in the KBr, which is used for FTIR analysis [34, 35].

2.2. DC Electrical Resistivity

Valuable information can be obtained from analysis of the temperature dependence of the dc electrical resistivity. Thus, many mechanisms can be invoked in analyzing the experimental data. Fig. 8 displays the temperature dependence of the d c electrical resistivity ρ (T) of the polycrystalline $La_{0.9-x}Y_xPb_{0.1}MnO_3$ (x = 0 and 0.1) ceramics in the temperature ranges from 100 to 400K. It is clear that the resistivity of the investigated samples increases up to a characteristic temperatures T_{MI}, where metal-insulator transition is highlighted and then decreases as the temperature continues to increase. Moreover, the ρ (T) curves can be divided into two distinct regions, metallic region (below T_{MI}) and insulating region (above T_{MI}). As a result of yttrium doping, the electrical resistivity of LYPMO sample increased substantially, and its temperature behavior approached that of ρ (*T*) for Y-free sample. And its peak value at $T=T_{MI}$ of the doped sample is one and half larger than that of the undoped one. Besides that, T_{MI} shifts to lower temperature as Y enhanced. Furthermore, the resistivity increases with the increase in Y^{3+} concentrations for whole range of temperature. This may be due to the interactions among various types of carrier species (electrons, holes, phonons) in the sample resulting in a strong scattering which in turn gives rise to elevated resistivity [36]. In other words, both samples display metal-insulator (M-I) transition having a peak at transition temperature T_{MI}. The peak value of resistivity at $T=T_{MI}$ increases and T_{MI} shifts to lower temperature with increased doping concentration, which infers that the Y doping leads to decreased conductivity in the samples. The variation of ρ and T_{MI} as the Y ions are substituted because of the increased distortion of the Mn-O-Mn bond and the increased disorder on the A-site of the $AMnO_3$ perovskite due to the small ionic radius of Y^{3+} compared to La^{3+} [37-39].

Qualitatively, the electrical resistivity in the low temperature of the metallic conductivity character below T_{MI} can be well expressed by the following equation [16, 40]:

$$\rho(T) = \rho(0) + AT^2.$$

The first term is being the residual resistivity arising from the temperature independent processes such as domain wall, grain boundary and vacancies [40] and the second term is related to the electron-electron contribution. Here, A is a constant, which provides the strength of electron-electron scattering [41]. The experimental resistivity data of present investigation in the metallic region where the electron-electron scattering process associated to spin fluctuation plays an important role in the present doped manganites [42], were fitted to the above equation as shown in Fig. 9. It can be seen from the figure that the theoretical and experimental curves match well.

Taking into account the variation of ρ (T) in the high temperature insulating (semiconducting) regime above T_{MI}, the electrical resistivity can be described by the following Arrhenius equation [43, 44]: $\rho = \rho_o \exp(E_\rho / K_B T)$ where the pre-exponential factor ρ_0 depends on the composition of the samples [45], K_B is the Boltzmann's constant, T is the absolute temperature and $E_{\square}$ represents the activation energy. The resistivity curves of both samples are plotted as ln (ρ) versus 1/T (Fig. 10). The calculated values of Eρ are 0.1002 ev for LPMO and 0.0867 ev for LYPMO. The difference in Eρ values suggests that the conduction in the insulating region is due to thermally assisted tunneling of charge carriers through the grain boundary barrier and transition from donor level to conduction band [36].

2.3. Dielectric Properties

For most applications in electronic materials, the dielectric properties of usual interest are the real (ε') and imaginary (ε'') components of the complex permittivity $\varepsilon^* = \varepsilon' + j\varepsilon''$. The real part of permittivity (ε') represents the polarizability of the material while the imaginary part (ε'') represents the energy loss due to polarization and ionic conduction [11]. The permittivity of a material reflects the molecular relaxation and transport processes of the material which depends on many parameters such as the structure of the materials, composition and synthesis method. In order to understand the influence of microstructure, composition and intergranular potential barrier on the electrical properties of ceramic, the frequency dependent real permittivity can be calculated using the relation: $\varepsilon' = Cd/\varepsilon_o A$ where *C* is effective capacitance, *d* sample thickness, ε_o free space permittivity, and *A* is the sample

area. The imaginary part of the permittivity (ε'') was calculated using the expression: $\varepsilon'' = \varepsilon' \tan\delta$ where: $\tan\delta = \tan(90-\varphi)$, is the dielectric loss tangent (dielectric loss factor). Dielectric loss factor is represented as dissipated energy in a dielectric system. It is considered to be caused by domain wall resonance. The frequency dependent of dielectric permittivity and the loss factor tan δ at room temperature for $La_{0.9-x}Y_xPb_{0.1}MnO_3$ in the frequency range of 75 kHz to 7 MHz are shown in Fig. 11. It is observed that the dielectric constant decreases as doping concentration increases. The decrease in dielectric constant indicates the formation of microstructure with LPMO grains surrounded by insulating grain boundaries and also suggests the existence of interface states in the grain boundaries. It is clear that the dielectric loss decreases with the increase in frequency for the samples which exhibit dispersion behavior similar to the dielectric constant. The value of tan δ is large at lower frequencies, while becomes lower at higher frequencies. It is evident that the overall values of tan δ are found to decrease with increasing the concentration of Y^{3+} ions for two samples. The observed dielectric behavior can be explained on the basis of Maxwell-Wagner interfacial type of polarization and Koops phenomenological theory [46]. According to this model, a dielectric medium is assumed to be made of well conducting grains which are separated by poorly conducting (or resistive) grain boundaries. The grain boundaries are found to be more effective at lower frequencies, while grains are effective at higher frequencies. The grain boundaries are formed during the sintering process due to the superficial reduction or oxidation of crystallites [47, 48]. The frequency independent behavior of both samples at higher frequency is just because of the charge carriers which are responsible for different mechanisms of polarization. Usually, the dipolar, electronic, ionic, and interfacial polarizations contributes to the dielectric constant of any material. At low frequencies, it is the dipolar and interfacial polarizations are effective to the dielectric constant. However, at higher frequencies the electronic polarization is effective and dipolar contribution becomes insignificant. The decrease in dielectric constant with increased frequency could be explained on the basis of dipole relaxation phenomenon [35]. Moreover, the dielectric materials polarize via one of the three mechanisms i.e. electronic, ionic or orientational polarization [49]. The electronic polarization and conduction mechanism are similar [50]. The increase in dielectric constant with increasing Y content may be attributed to the increased interfacial polarization due to large volume fraction of grain boundaries as a consequence of decrease in grain sizes [13]. The higher value of dielectric permittivity at lower frequencies is due to presence of different type of polarization in particular space charge polarization. Whereas, nearly constant value of it was observed at higher frequency due absence of space charge polarization [51].

3. Conclusion

A detailed investigations of microstructural, electrical resistivity and dielectric properties of polycrystalline LPMO and LYPMO samples synthesized by ceramic technology have been investigated using FESEM, EDS, XRD, Raman, FTIR, dc electrical resistivity and dielectric measurements. In FESEM images, all samples show clear grain and grain boundary. The grain growth was demoted by the substitution of Y ions. EDS spectra confirmed the presence of all the constituents. Both compounds synthesized were found to have single phase a rhombohedral structure. XRD and Raman spectra confirm a rhombohedral $R\bar{3}c$ structure of undoped and Y-doped LPMO. The partial substitution of Y^{3+} in LPMO slows down the oxygen ion motion consequently reducing grain growth and resulting in a decrease in the average grain size. The interaction between the Y atoms and the support LPMO hinders the crystallization, which is reflected in the reduction of peak intensity. The Raman observations are also supported by XRD and FTIR studies. The electrical resistivity of both samples versus temperature shows the similar trend. Substitution of lanthanum by yttrium results in a considerable increase of the resistivity ρ, as well as the reduction of T_{MI}. This behavior may be due to the structural distortion associated to a decrease in the average radius $\langle A_i \rangle$ of the A-cation site in $La_{1-x}Y_xPb_{0.1}MnO_3$. The electrical resistivity of these samples in metallic regime (below T_{MI}) may be due to the quadratic temperature (T^2) dependence, while in the high temperature semiconducting regime (above T_{MI}) the conduction is due to thermally activated conduction (TAC) law. The dielectric constants of both samples increase with the decrease in frequency at lower frequencies and remains almost unchanged at higher frequencies. It is also observed that tan δ for LPMO and LPYMO increases with rise in frequency.

References

[1] Dhahri, A., Rhouma, F. I. H., Dhahri, J., Dhahri, E., and Valente, M. A., 2011. "Structural and electrical characteristics of rare earth simple perovskite oxide La0.57Nd0.1Pb0.33Mn0.8Ti0.2O3." *Solid State Communications*, vol. 151, pp. 738–742.

[2] Thakur, S., Pandey, O. P., and Singh, K., 2013. "Structural and dielectric properties of Bi1-xSrxMnO3." *Ceramics International*, vol. 39, pp. 6165-6174.

[3] Alvydas, L., Khartsev, S. I., and Alex, G., 2000. "Tailoring the colossal magnetoresistivity: La0.7(Pb0.63Sr0.37)0.3MnO3 thin-film uncooled bolometer." *Appl. Phys. Lett.*, vol. 77, p. 756.

[4] Chen, P., Xing, D. Y., and Du, Y. W., 2001. "Positive magnetoresistance from quantum interference effects in perovskite-type manganites." *Phys. Rev.*, vol. B64, p. 104402.

[5] Dyakonov, V., 2009. "Nanoparticle size effect on the magnetic and transport properties of (La 0.7Sr0.3)0.9Mn1.1O3 manganites, Low Temp." *Phys.*, vol. 35, p. 568.

[6] Lopez-Quintela, M. A., Hueso, L. E., Rivas, J., and Rivadulla, F., 2003. "Intergranular magnetoresistance in nanomanganites." *Nanotechnology*, vol. 14, p. 212.

[7] Mahendiran, R., Mahesh, R., Raychaudhuri, A. K., and Rao, C. N. R., 1995. "Room temperature giant magnetoresistance in La1-xPbxMnO3,J. Phys. D. 20." *Appl. Phys.*, vol. 28, p. 1743.

[8] Srinivasan, G., V., S. B., and Seehra, M. S., 1995. "Magnetic properties of radio frequency sputtered thin films of La-Pb-Mn oxides." *Appl. Phys. Lett.*, vol. 67, p. 2090.

[9] Young, S. L., Chen, Y. C., Chen, H. Z., Horng, L., and Hsueh, J. F., 2002. "Effect of the Substitutions of Ni+3, Co+3, and Fe+3 for Mn+3 on the Ferromagnetic States of the La0.7Pb0.3MnO3 Manganite." *J. Appl. Phys.*, vol. 91, pp. 8915-8917.

[10] Eerenstein, W., Mathur, N. D., and Scott, J. F., 2006. "Multiferroic and magnetoelectric materials." *Nature*, vol. 442, pp. 759-765.

[11] Khor, S. F., Talib, Z. A., Sidek, H. A. A., Daud, W. M., and Ng, B. H., 2009. "Effects of ZnO on dielectric properties and electrical conductivity of ternary zinc magnesium phosphate glasses." *American J. Appl. Sci.*, vol. 6, pp. 1010-1014.

[12] Rodríguez-Carvajal, J., 2001. "Recent developments of the program FULLPROF, Commission on powder diffraction (IUCr), Newsletter." vol. 26, pp. 12–19.

[13] Fakhrul, T., Mahbub, R., Chowdhury, N., Mohd, K. Q. D., and Sharif, A., 2015. "Structural, dielectric and magnetic properties of Ta-substituted Bi0.8La0.2FeO3 multiferroics." *J. Alloys and Compd.*, vol. 622, pp. 471–476.

[14] Blagoev, B. S., Terzieva, S. D., Nurgaliev, T. K., Shivachev, B. L., Zaleski, A. J., Mikli, V., Staneva, A. D., and Stoyanova-Ivanova, A. K., 2013. "Magnetic and transport characteristics of oxygenated polycrystalline La0.6Pb0.4MnO3." *J. Magn. Magn. Mater.*, vol. 329, pp. 34–38.

[15] Mtiraoui, N., Dhahri, A., Oumezine, M., Dhahri, J., and Dhahri, E., 2011. "Effects of nonmagnetic silver Ag doping on the structural, magnetic and electric properties in La0.67Pb0.33MnO3 manganese oxides." *J. Magn. Magn. Mater.*, vol. 323, p. 2831.

[16] Bebenin, N. G., Zainultina, R. I., Maikov, S. V., Ustinov, V. V., and Mukovskii, Y. M., 2010. "Effect of yttrium doping on the resistivity and magnetoresistance of La0.80Sr0.20MnO3." *The Physics of Metals and Metallography*, vol. 110, pp. 463-469.

[17] Sun, P., Wang, C., Zhou, X., Cheng, P., Shimanoe, K., Lu, G., and Yamazoe, N., 2014. "Cu-doped α-Fe2O3 hierarchical microcubes: Synthesis and gas sensing properties." *Sensors and Actuators*, vol. B 193, pp. 616-622.

[18] De Keiyser, T. H., Langford, J. I., Mittemeijer, and Vogels, A. B. P., 1982. "Use of the Voigt function in a single-line method for the analysis of X-ray diffraction line broadening." *J. Appl. Cryst.*, vol. 15, pp. 308-314.

[19] Dwivedi, G. D., Shukla, K. K., Shahi, P., Ghosh, A. K., Nigam, A. K., and Sandip, C., 2013. "Effect of Y-doping on the transport and magnetic properties of La0.5Sr0.5CoO3 and La0.7Sr0.3CoO3." *J. Mater. Sci.*, vol. 48, pp. 1997-2001.

[20] Liu, Y. and MacManus-Drisoll, J. L., 2009. "Impurity control in Co-doped ZnO films through modifying cooling atmosphere." *Appl. Phys. Lett.*, vol. 94, p. 022503.

[21] Carron, M., de Andrés, A., Martínez-Lope, M. J., Casais, M. T., and Alonso, J. A., 2002. "Raman phonons as a probe of disorder, fluctuations, and local structure in doped and undoped orthorhombic and rhombohedral manganites." *Phys. Rev.*, vol. B66, p. 174303.

[22] Haumont, R., Kreisel, J., Bouvier, P., and Hippert, F., 2006. "Phonon anomalies and the ferroelectric phase transition in multiferroic BiFeO3." *Phys. Rev.*, vol. B73, p. 132101.

[23] Luo, L., Wei, W., Yuan, X., Shen, K., Xu, M., and Xu, Q., 2012. "Multiferroic properties of Y-doped BiFeO3." *J. Alloys & Compd.*, vol. 540, pp. 36-38.

[24] Dodiya, N. and Varshney, D., 2013. "Structural properties and Raman spectroscopy of rhombohedral La1-xNaxMnO3 ($0.075 \leq x \leq 0.15$)." *J. Molecular Structure*, vol. 1031, pp. 104-109.

[25] De Marzi, G., Trodahl, H. J., Bok, J., Cantarero, A., and Sapina, F., 2003. "The effect of Cu substitution on the A1g mode of La0.7Sr0.3MnO3 manganites." *Solid State Commun.*, vol. 127, pp. 259-264.

[26] Dubroka, A., Humlicek, J., Abrashev, M. V., Popovic, Z. V., Sapina, F., and Cantarero, A., 2006. "Raman and infrared studies of La1−ySryMn1−xMxO3 (M=Cr, Co, Cu, Zn, Sc or Ga): Oxygen disorder and local vibrational modes." *Phys. Rev.*, vol. B76, p. 224401.

[27] Malavasi, L., Alessandri, I., Mozzati, M. C., Ghigna, P., Chiodelli, G., and Azzonib, C. B., 2003. "Preparation, structural and magnetic characterization of RF-sputtered La1−xNaxMnO3±δ thin films manganites, G. Flora,." *Phys. Chem. Chem.*, vol. 5, pp. 2274-2278.

[28] Abrashev, M. V., Backstrom, J., Borjesson, L., Pissas, M., Kolev, N., and Iliev, M. N., 2001. "Raman spectroscopy of the charge- and orbital-ordered state in La0.5Ca0.5MnO3." *Phys. Rev.*, vol. B64, p. 144429.

[29] Iliev, M. N. and Abrashev, M. V., 2001. "Raman phonons and Raman Jahn–Teller bands in perovskite-like manganites." *J. Raman Spectrosc.*, vol. 32, p. 805.

[30] Liu, H. L., Her, J. L., Shen, C. H., and Liu, R. S., 2003. "Optical studies of lattice and charge excitations in La1.2(Sr1.8−xCax)Mn2O7." *J. Appl. Phys.*, vol. 93, pp. 6894-6896.

[31] Bhowmik, R. N. and Naresh, N., 2010. "Structure, ac conductivity and complex impedance study of Co_3O_4 and Fe_3O_4 mixed spinel ferrites." *Int. Eng. Sci. Technol.*, vol. 2, pp. 40-52.

[32] Ravi, S. and Karthikeyan, A., 2014. "Effect of calcination temperature on La0.7Sr0.3MnO3 nanoparticles synthesized with modified sol-gel route." *Physics Procedia*, vol. 54, pp. 45 – 54.

[33] Regaieg, Y., Koubaa, M., Cheikhrouhou, K. W., Cheikhrouhou, A., Sicard, L., Ammar-Merah, S., and Herbst, F., 2013. "Structure and magnetocaloric properties of La0.8Ag0.2−xKxMnO3 perovskite manganites." *Materials Chemistry and Physics,* vol. 132, pp. 839– 845.

[34] Rahimi, M., Kameli, P., Ranjbar, M., Hajihashemi, H., and Salamati, H., 2012. "The effect of zinc doping on the structural and magnetic properties of Ni12xZnxFe2O4." *J. Mater. Sci.,* vol. 48, pp. 2969-2976.

[35] Varshney, D., Kumar, A., and Verma, K., 2011. "Effect of A site and B site doping on structural, thermal, and dielectric properties of BiFeO3 ceramics." *J. Alloys and Compd.,* vol. 509, pp. 8421– 8426.

[36] Azam, A., Jawad, A., Ahmed, A. S., Chaman, M., and Naqvi, A. H., 2011. "Structural, optical and transport properties of Al3+ doped BiFeO3 nanopowder synthesized by solution combustion method." *J. Alloys and Compd.,* vol. 509, pp. 2909–2913.

[37] Altintas, S. P., Amira, A., Mahamdioua, N., Varilci, A., and Terzioglu, C., 2011. "Effect of Eu doping on structural and magneto-electrical properties of La0.7Ca0.3MnO3 manganites." *J. Alloys and Compd.,* vol. 509, pp. 4510–4515.

[38] Damay, F., Macmanus-Driscoll, and Cohen, L. F., 2000. *Influence of microstructure and magnetic state on low temperature magnetoresistance properties of bulk La0.7-xYXCao.3MnO3, R. Cloots et al. (eds.), Supermaterials*. Kluwer Academic Publishers, pp. 57-65.

[39] Shaikh, M. W., Mansuri, I., Dar, M. A., and Dinesh, V., 2015. "Structural and transport properties of La1-xAgxMnO3(x = 0.075,0.1,0.125 and 0.15) manganites." *Materials Science in Semiconductor Processing,* vol. 35, pp. 10-21.

[40] Bebenin , N. G., Zainullina, R. I., Chusheva, N. S., Elokhina, L. V., Ustinov, V. V., and Mukovskii, Y. M., 2007. "Transport Phenomena in the La0.72Ba0.28MnO3 Single Crystal." *The Physics of Metals and Metallography*, vol. 103, pp. 261–269.

[41] Varshney, D., Mansuri, I., Kaurav, N., Lung, W. Q., and Kuo, Y. K., 2012. "Influence of Ce doping on electrical and thermal properties of La0.7-xCexCa0.3MnO3 (0.0≤ x≤ 0.7) manganites." *J. Magnet. Magnet. Mater.*, vol. 324, pp. 3276–3285.

[42] Craus, M. L., Islamov, A. K., Anitas, E. M., Cornei, N., and Luca, D., 2014. "Microstructural, magnetic and transport properties of La0.5Pr0.2Pb0.3-xSrxMnO3 manganites." *J. Alloys and Compd.,* vol. 592, pp. 121–126.

[43] Abdel-Latif, I. A. and Saleh, S. A., 2012. "Effect of iron doping on the physical properties of europium manganites." *J. Alloys and Compd.,* vol. 592, p. 12.

[44] Burzo, E., Balasz, I., Isobe, M., and Ueda, Y., 2012. "Physical properties of La1-xPbxMnO3 perovskites with $0.24 \leq x \leq 0.40$." *J. Alloys and Compd.,* vol. 535, pp. 129–137.

[45] Saleh, S. A., 2014. "Enhancement of the power factor of Pb1–xSnxTe ($0.00 \geq x \geq 0.08$) alloys." *Philosophical Magazine,* vol. 94, pp. 3183-3194.

[46] Hassan, M. M., Ahmed, A. S., Chaman, M., Wasi, K., Naqvi, A. H., and Ameer, A., 2012. "Structural and frequency dependent dielectric properties of Fe3+ doped ZnO nanoparticles." *Mater. Res. Bull.,* vol. 47, pp. 3952–3958.

[47] El Hiti, M. A., 1999. "Dielectric behaviour in Mg–Zn ferrites." *J. Magn. Magn. Mater.*, vol. 192, pp. 305–313.

[48] Reddy, P. V. and Rao, T. S., 1982. "Dielectric behaviour of mixed Li-Ni ferrites at low frequencies." *J. Less Common Met.,* vol. 86, pp. 255–261.

[49] Mahmoud, A., Warsi, M. F., Ashiq, M. N., and Sher, M., 2012. "Improvements in electrical and dielectric properties of substituted multiferroic LaMnO3 based nanostructures synthesized by co-precipitation method." *Mater. Res. Bull.,* vol. 47, pp. 4197-4202.

[50] Iqbal, M. J., Ashiq, M. N., and Gul, I. H., 2010. "Physical, electrical and dielectric properties of Ca-substituted strontium hexaferrite (SrFe12O19) nanoparticles synthesized by co-precipitation method." *J. Magn. Magn. Mater.*, vol. 322, pp. 1720-1726.

[51] Mohanty, S., Choudhary, R. N. P., Padhee, R., and Parida, B. N., 2014. "Dielectric and impedance spectroscopy of BiFeO3–NaTaO3 multiferroics." *Ceramics International,* vol. 40, pp. 9017-9025.

Fig-1. FESEM images of $La_{0.9-x}Y_xPb_{0.1}MnO_3$ (x = 0 and 0.1)

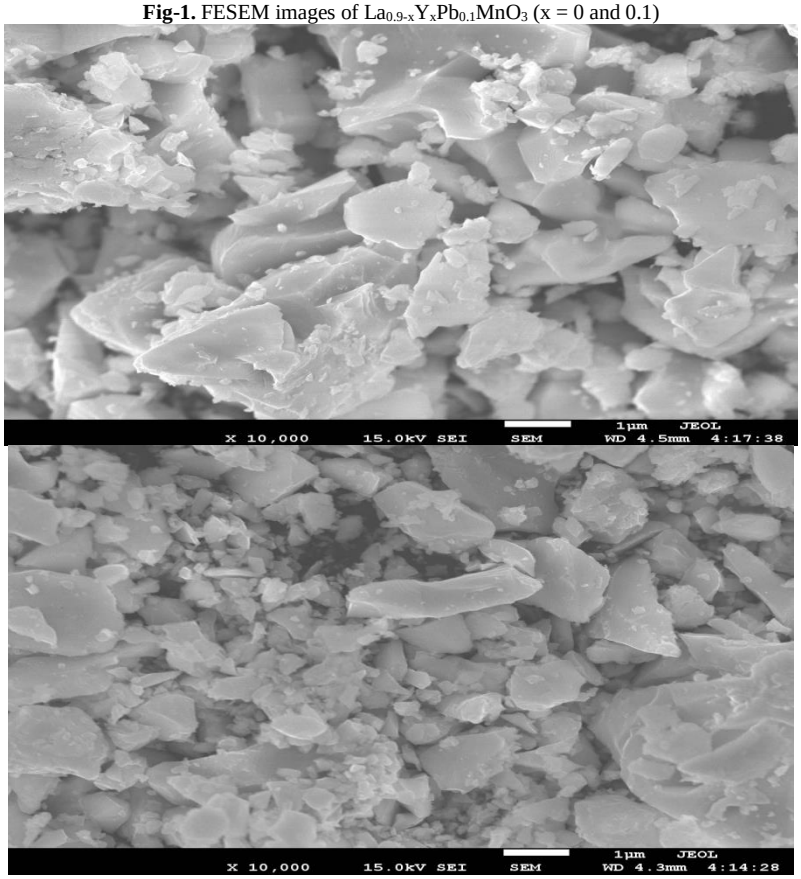

Fig-2. EDS plots for $La_{0.9-x}Y_xPb_{0.1}MnO_3$ (x = 0 and 0.1)

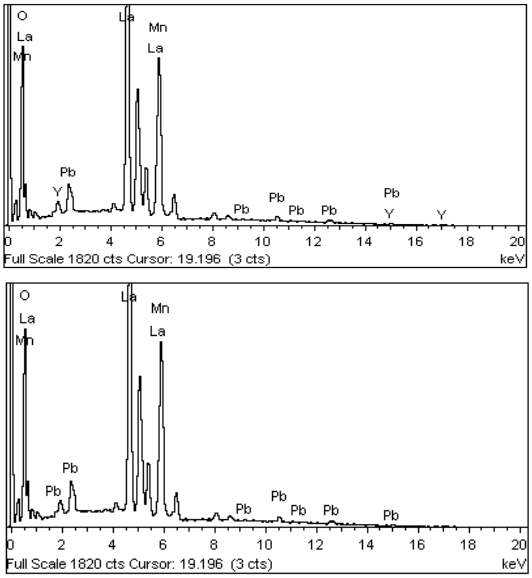

Fig-3. XRD patterns of $La_{0.9-x}Y_xPb_{0.1}MnO_3$ (x = 0 and 0.1).

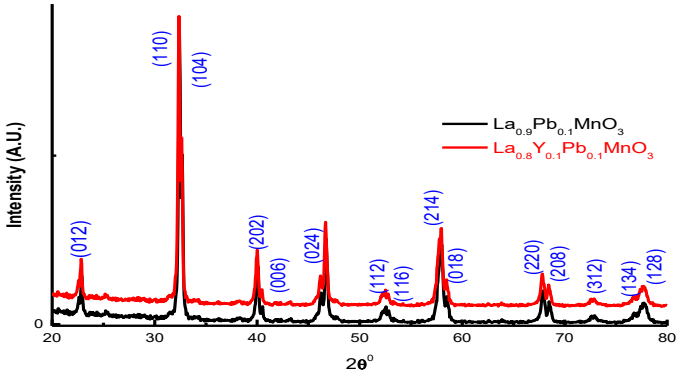

Fig-4. Rietveld plot of XRD data for polycrystalline $La_{0.9-x}Y_xPb_{0.1}MnO_3$ (x = 0 and 0.1) at 300 K.

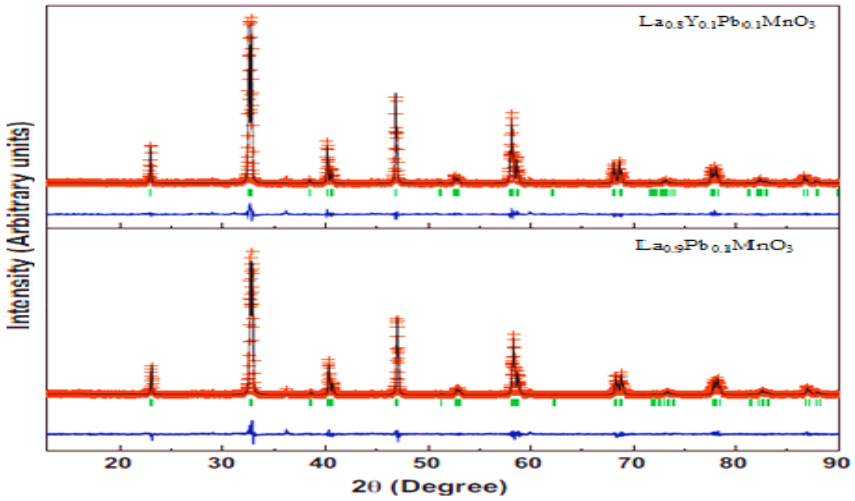

Fig-5. Room temperature Raman spectra of $La_{0.9-x}Y_xPb_{0.1}MnO_3$ (x = 0 and 0.1)

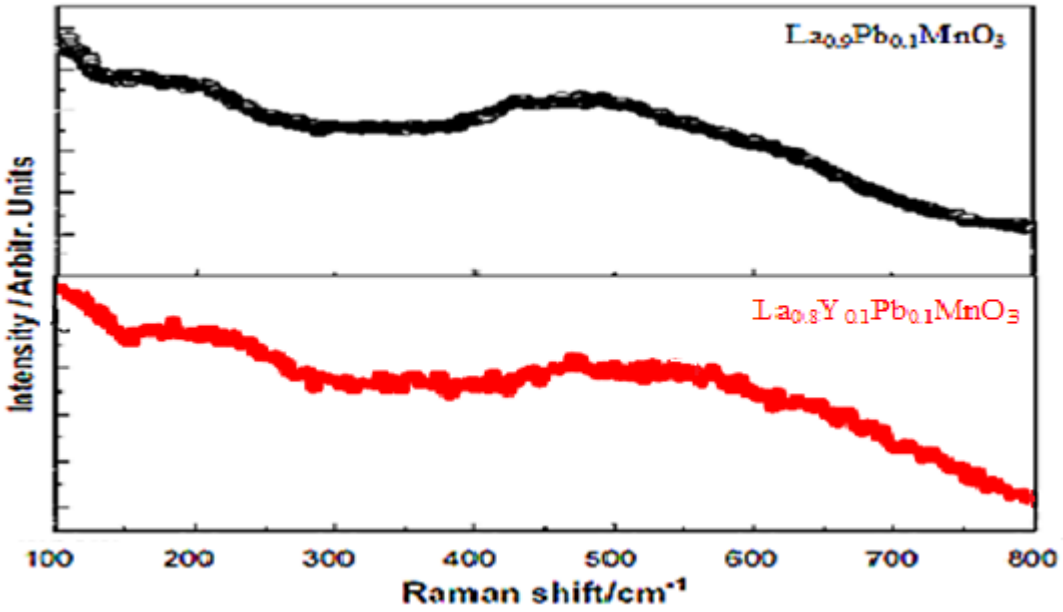

Fig-6. Raman spectrum of both samples fitted by using Lorentzian function

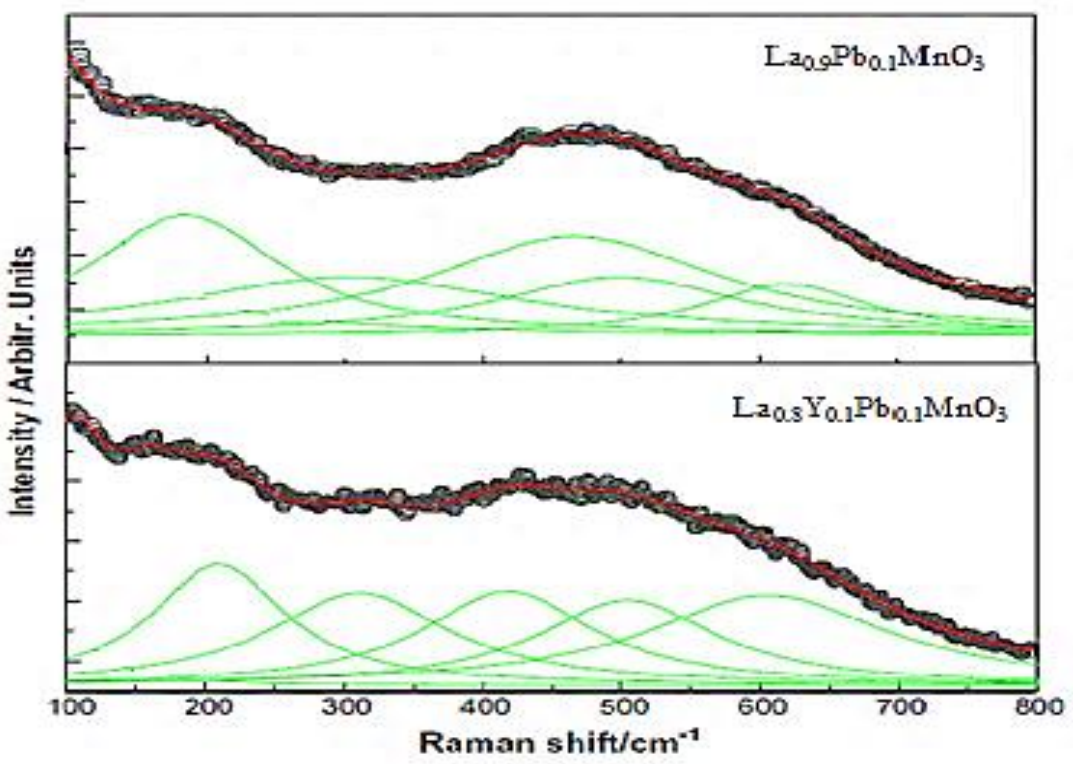

Fig-7. FTIR spectrum for Y doped LPMO samples

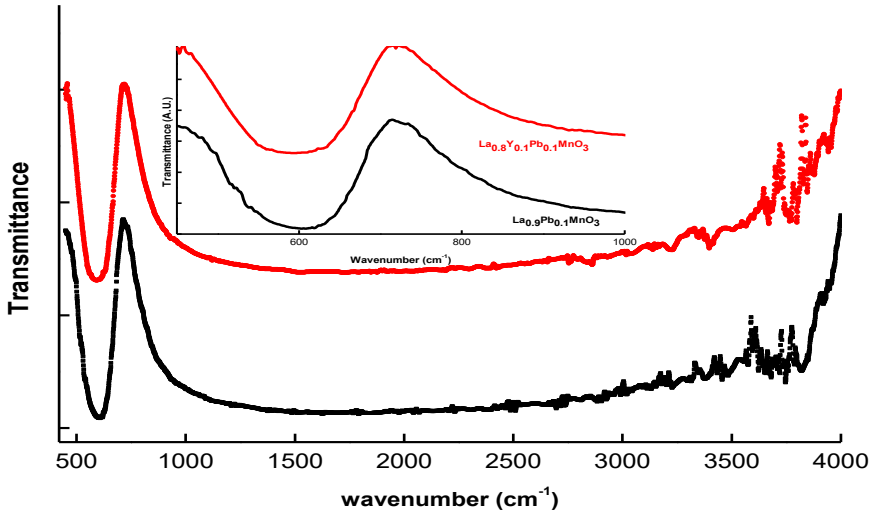

Fig. 7

Fig-8. Temperature dependence of the resistivity for different ceramics

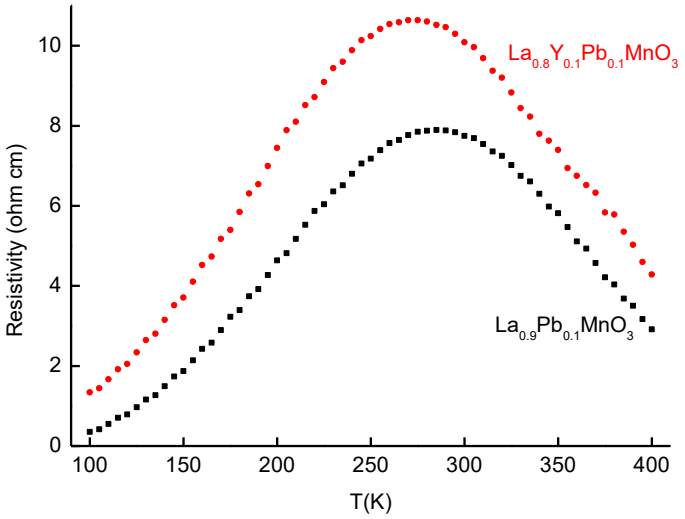

Fig-9. Dependence of the resistivity data on T^2 for both samples

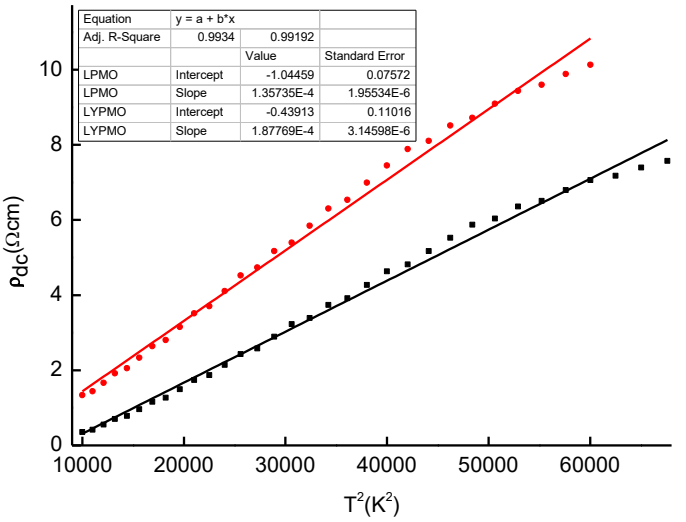

Fig-10. Plot of ln (ρ) vs.1000/T for for both samples

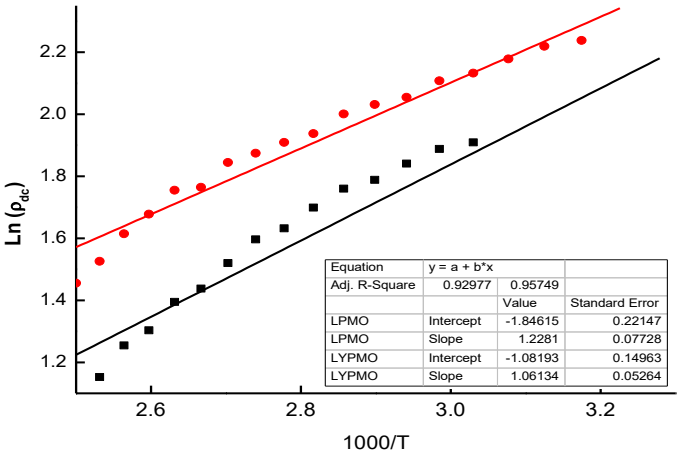

Fig-11. Frequency dependence of (a) dielectric constant and (b) energy loss for two ceramics

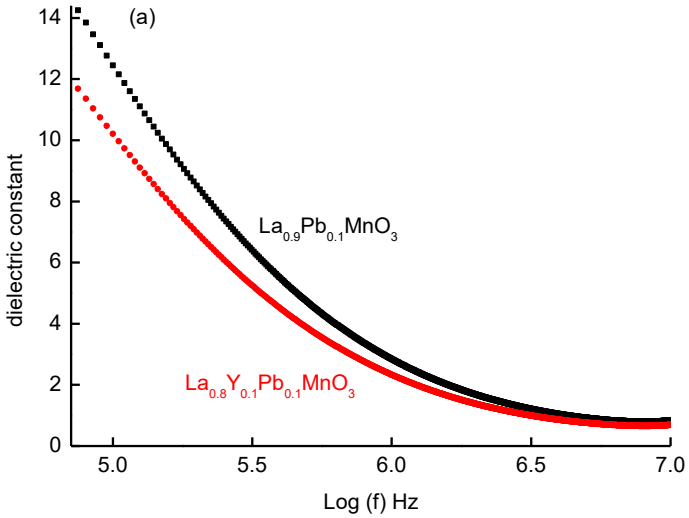

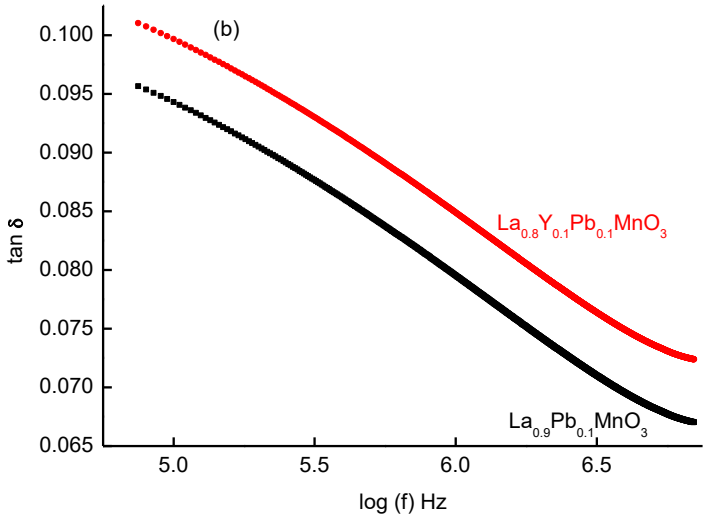

Table-1. Crystallographic data of present samples

Sample Code	LPMO	LYPMO
a (nm)	0.55002 (5)	0.54944 (3)
c (nm)	1.33351 (4)	1.32641 (5)
V (nm^3)	0.4034161	0.400422
R_P	16.55	16.55
R_{WP}	20.55	20.55
GOF	1.65	1.65